Journal of Ceramic Processing Research. Vol. 19, No. 2, pp. 111~118 (2018)

J O U R N A L O F
Ceramic Processing Research

Property evaluation of Cu-based metal-hybrid material prepared by chemical reaction and pulse current activated sintering process

Jun-Ho Jang[a,b], Hyun-Kuk Park[a], Jeong han Lee[a], Jae-Won Lim[b] and Ik-Hyun Oh[a]

[a]*Korea Institute of Industrial Technology (KITECH), 1110-9 Oryong-dong, Buk-gu, Gwangju-city 500-480, Korea*

[b]*Division of Advanced Materials Engineering, Chonbuk National University, Jeonbuk 561-756, Korea*

In this paper, Cu-coated graphite sintered body for weight reduction and high thermal conductivity was fabricated using a chemical reaction process and pulsed current activated sintering process. First, 4 g of coarsening graphite powders, which was treated using an activation and wetting process, was added to an aqueous solution of copper (Cu) sulfate; also, 35 g of zinc (Zn) powders was added as a transposition solvent to the aqueous solution, and stirred for 1 h for a transposition reaction. After the addition of the fabricated powders mixture to a 75 wt.% DI water : 10 wt.% H_3PO_4 : 10 wt.% H_2SO_4 : 5 wt.% mixture, tartaric acid was added to the aqueous solution to produce a passivating oxide film, followed by drying for 24 h. The low-intensity oxide peak of the XRD pattern of the fabricated powders was due to the suitable Zn powder content. The Cu-coated graphite powder was used to carry out direction control for high thermal conductivity. Cu-coated graphite sintered bodies were fabricated using a pulsed current activated sintering (PCAS) process. The Cu-graphite sintered bodies were sintered at 850 °C with heating rate steps of 20 and 30 °C/min, respectively. The Cu-coated graphite powders and compacts were evaluated using FE-SEM, EDS, XRD, TEM, particle analysis, Archimedes' method, electronic conductivity, thermal coefficient, and thermal conductivity.

Key words: Chemical reaction process, Cu-coated graphite, Microstructures, Electric conductivity, Thermal conductivity.

Introduction

Information processing abilities for bulk storage and highly integrated electronics are greatly needed in industrial applications in terms of optical communications, photoelectrons, LEDs, and RF packages; however compared to other applications, the application components generate a large amount of heat. It is very important to effectively transmit and control heat for application performances. Components such as electric and electronic equipment are characterized by electron movements; therefore, the more the integration and the higher the output, the more heat that the electric and electronic equipment generate. When the generated heat cannot be rapidly released, the heat-based deterioration of the outside of the electric and electronic equipment becomes severe, and the performance and lifetime of the corresponding product are drastically degraded, thereby reducing the reliability of the product [1-8]. To solve this problem, the heat is conventionally emitted using a heat-sink material made of copper (Cu), whereby excellent thermal conductance is provided, and a metal material like aluminum (Al) is applied to the outside of the electric and electronic equipment. But, when a metal is used as the heat-sink material, the material easily drops out, due to the cracking that is caused by the difference of the thermal-expansion coefficient between the heat-sink material and the junction-base metal; consequently, either the heat-sink material is welded to the part where the phenomenon is occurring, or the large mass generates excessive degradation of the product, which metal-characteristic property is due to the high thermal-expansion coefficient.

A non-metal-group inorganic material like silicon carbide (SiC) or aluminum nitride (AlN) is lightweight in comparison with aluminum (Al) or Cu, and the low thermal-expansion coefficient confirms its suitability for use as a substrate material. However, a disadvantage is that the thermal conductivity of such materials is less than 200 W/mk; therefore, carbon (C)-base composite materials (e.g., C fibers, C nanotubes, and graphite) are proposed to improve this problem.

In this paper, Cu-coated graphite powders were fabricated according to a chemical-reaction process, and Cu-coated sintered bodies were fabricated using a pulsed current-activated sintering method to achieve a low thermal expansion coefficient and high thermal conductivity. The Cu-coated graphite powder and compacts were evaluated using field-emission scanning electron microscopy (FE-SEM), energy dispersive X-ray spectroscopy (EDS), X-ray diffraction (XRD), particle analysis, and Archimedes' method.

*Corresponding author:
Tel : +82-62-600-6180
Fax: +82-62-600-6149
E-mail: ihoh@kitech.re.kr

Experimental Procedure

In the chemical reaction process for which graphite powder (Qingdao Kropfmuehl, > 99.5%, d(0.5) 7.2 μm) was used, the Cu was displaced from the Cu-sulfate solutions by zinc (Zn); a description of the mechanisms involved was provided in [reference]. Briefly, the displacement of the Cu from the Cu-sulphate solution with the use of Zn-reducing agents can be achieved as follows:

$$CuSO_4(aq) + Zn(s) \rightarrow ZnSO_4(aq) + Cu(s) \quad (1)$$

The Cu-sulfate solution and glacial acetic acid (AcOH) are used for the graphite powder coatings. Upon the completion of the chemical reaction, the displaced metal ion (Cu^{2+}) becomes neutralized; however for a brief initial period, the charge of the Cu^{2+} is positive. After a reaction with acid, graphite powder typically comprises polar surface groups. In the present case, the graphite powder after the reaction with the AcOH comprises a carboxyl group (R-COOH), leaving the powder with a negative charge, and coating the Cu^{2+} with the positive charge on the powder. The AcOH also maintains the activated state of the powder surface, so that the coating was uniform [9].

Fig. 1 shows the FE-SEM imagery and XRD patterns of graphite powder, wherein the graphite powder is flake-shaped, and only graphite phase peaks are evident. The graphite powder size was over 100 μm, and the reason for using large amounts of powder was to facilitate directional control. First, the 4 g of graphite powder was subject to an activation treatment in an electric furnace at 400 °C for 1 hr; this treatment barely affected the mechanical properties of the graphite powders within the experimental accuracy. The 4 g of graphite powder was then dipped in 2 ml of he AcOH to further improve the wettability of the graphite surface in relation to the metal that was to be coated. Subsequently, 600 ml of a 1 M Cu-sulfate solution was added to the activator bath, and 35 g displacing agent (zinc powder) was added to displace the metal from the solution. The reason for setting 1 M of Cu-sulfate solution and 4 g graphite powders were to set the volume ratio of graphite and copper to be 5 : 5. The bath was stirred well to uniformly disperse the powders in the solution for 1 hr. The completion of the chemical-reaction process was indicated by the color changes of the solution and the powders. The Cu-coated graphite powder was then treated in an acid-stabilizer bath (75% D.I water + 10% H_2SO_4 + H_3PO_4 + 5% tartaric acid) for 20 min, thereby reducing the tarnishing of the coated Cu. The coated powders were washed thoroughly with water prior to an 80 °C drying. The uniformity of the coating was studied according to the microstructure, and the thickness of the coating layer was studied by particle analysis. The compositions of the graphite and Cu were studied by EDS, and this was followed by the study of the phase of the Cu-coated graphite powder by XRD.

After the Cu was coated on the graphite powder by the chemical reaction process, the graphite powder was direction controlled by a vibrator for 10, 20, and 30 min. With the treatment of vibration for powder, the graphite powder was sintered by a pulsed current activated sintering (PCAS) method. Fig. 2 shows a schematic of the apparatus that was used for the PCAS process, which includes a 25 V, 1,000 A dc-power supply (providing a pulsed current for 12 ms with an off time of 2 ms through the sample and the die) and a 10 ton uniaxial press. First, the system was evacuated, followed by the application of a standard uniaxial pressure. A DC pulse current was then activated, and maintained until a negligible densification rate was obtained, as indicated by the observed shrinkage of the sample. The sample shrinkage was measured in real time using a linear gauge for the vertical displacement. The temperature was measured using a K-type thermocouple. Depending on the heating rate, the electrical and thermal conductivities of the compact, the relative density of the compact, and the temperatures on the surface and in the center of the sample could differ. The sintering-treatment heating rates were 20 and 30 °C. After the temperature reached 600 °C, a uniaxial pressure of

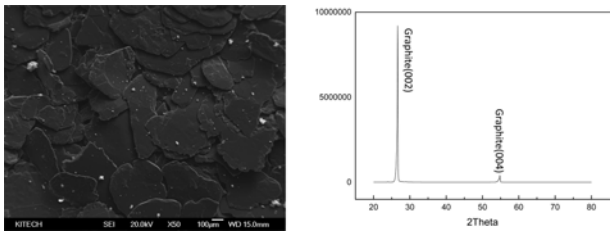

Fig. 1. FE-SEM image and XRD pattern of Graphite powder(100 μm over).

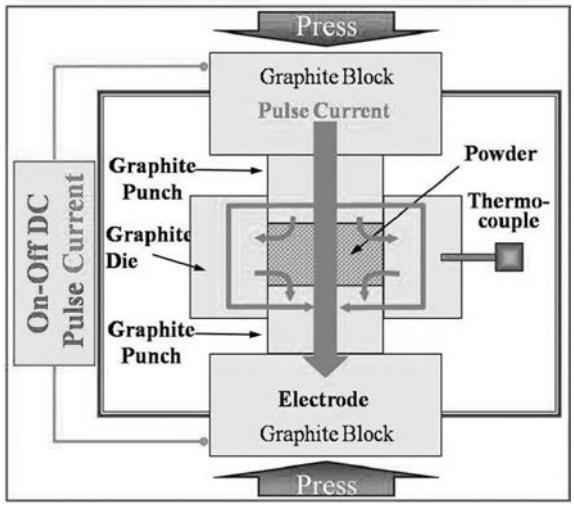

Fig. 2. Schematic diagram of apparatus for PCAS process.

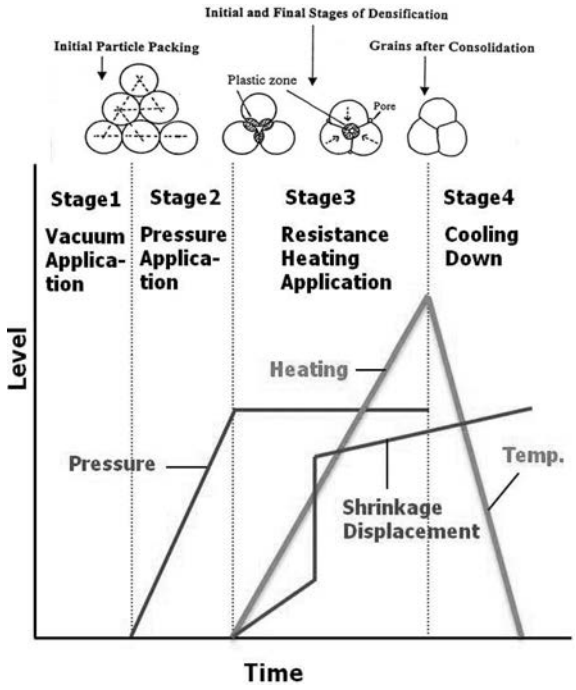

Fig. 3. Schematic representation of temperature, pressure and shrinkage displacement profile during PCAS process.

60 MPa was applied. After the completion of the sintering treatment at 850 ºC, the current was turned off, and the sample was allowed to cool to room temperature. The entire densification process for which the PCAS technique was used consists of the following four major control stages: chamber evacuation, pressure application, power application, and cool-down. Fig. 3 shows a schematic of the four major sintering stages. The relative densities of the sintered samples were measured using Archimedes' method. The compositional and microstructural analyses of the compacts were studied by XRD and FE-SEM. The electronic conductivity was studied using a non-destructive tester, and the thermal conductivity was studied by laser flash analysis (LFA) and differential scanning calorimetry (DSC).

Results and Discussion

For the particle analysis, initial graphite powder and Cu coated graphite powder were used. The results of the particle analysis (Fig. 4) show a decrease of the particle size of the Cu-coated graphite powder from the initial graphite particle size of d(0.5) 242.8 μm to d(0.5) 85.4 μm. The amount of the displacement in the aqueous solution according to the reducing-agent saturation was calculated as follows:

$$qG_A = 100/(1+(X_B M_B/X_A M_A)) \quad (2)$$

where, G_A is the weight percent of A, X_A is the atomic percent of A, X_B is the atomic percent of B, M_A is the atomic weight of A, and M_B is the atomic weight of B. Eq.(2) is here used to supersaturate the Cu with a 35.7 wt.% reducing agent, and this accounts for the inconsistent progression of the displacement process.

Fig. 5 shows the microstructure imagery and XRD pattern of the Cu-coated graphite powder at different magnification, wherein the Cu-coated particles are almost irregularly shaped. In the microstructure imagery, the bright area is the Cu, and the dark area is the graphite; since the heavy elements (high atomic number) backscatter the electrons more strongly than do the light elements (low atomic number), they appear brighter in microstructure images. The backscattered electrons (BSEs) are used to detect the contrast between the areas with different chemical compositions. Fig. 5 (a) shows the mixture of copper and graphite powder. Fig. 5(b)

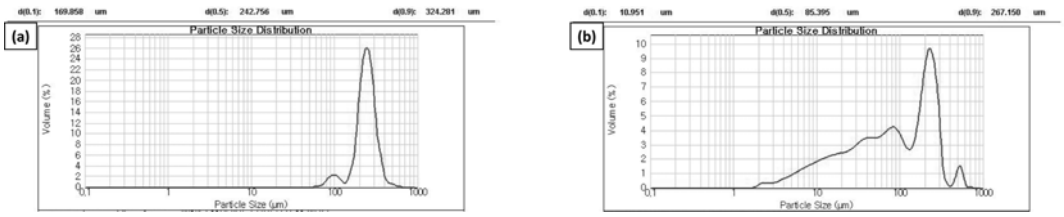

Fig. 4. Particle analysis of graphite powder and copper-coated graphite powder; (a) Graphite powder, (b) Copper-coated graphite powder.

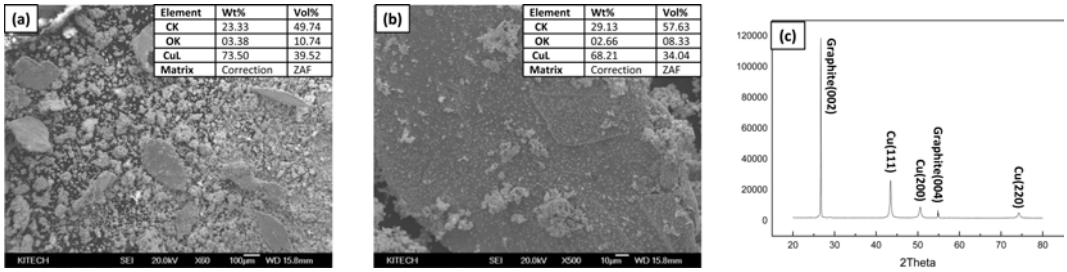

Fig 5. XRD pattern, Microstructure and EDAX analysis of copper-coated graphite powder at different magnification; (a) (x60) magnification, (b) (x500) magnification and (c) XRD pattern.

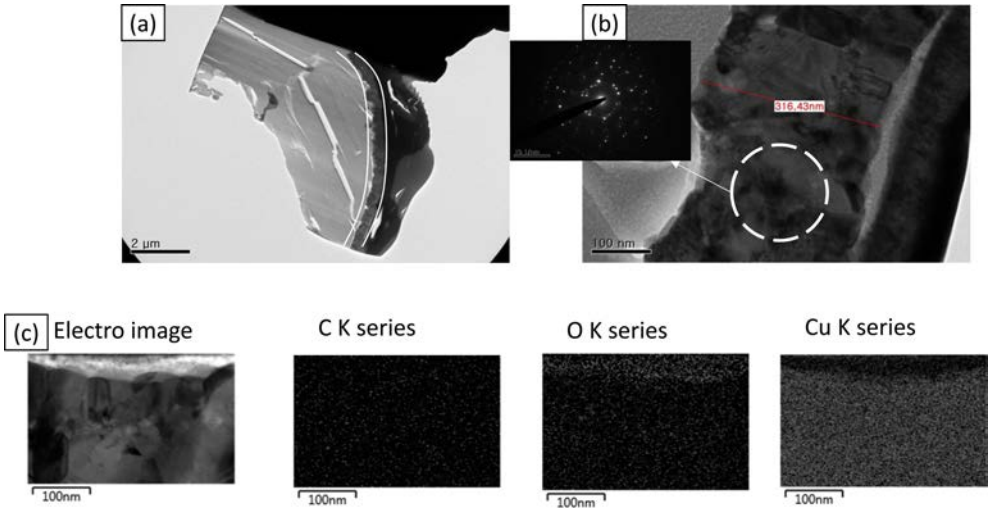

Fig. 6. TEM image of copper-coated graphite powder; (a) Total image, (b) diffraction pattern and Coating thickness and (c) Mapping.

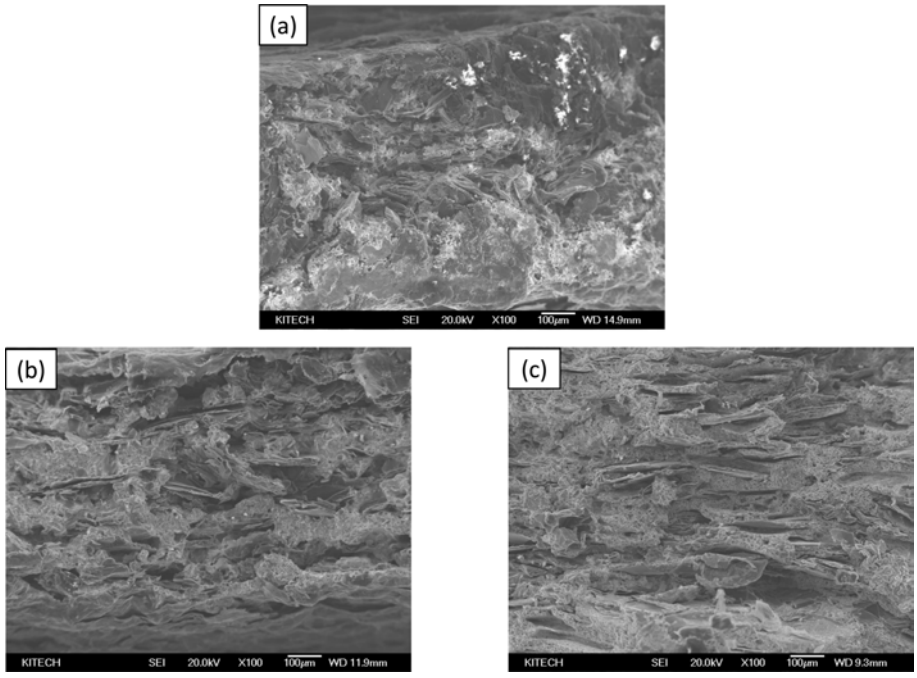

Fig. 7. Microstructure of controlled direction copper-coated graphite powder at different time; (a) 10 min., (b) 20 min. and (c) 30 min.

shows that copper coating was generally coated in a single graphite phase, and agglomerated copper locally existed. The microstructure shows that transposed copper ions from copper sulfate solution were coated with pre-treated graphite powders, and Cu-coated graphite powder and copper powder coexisted. The results of the EDS analyses show that the Cu-coated graphite powder does not affect the initial volume ratio.

XRD patterns of the Cu-coated graphite powder in Fig. 5(c) reveal the graphite (002) and (004), and Cu (111), (200), and (220) peaks for the Cu-coated graphite powder, indicating that no impurities were added during the chemical-reaction process.

The XRD patterns show that beyond saturation reducing agents were added, and the Cu oxides were fabricated, which decrease the powder properties. The grain size and the internal strain were calculated using the Stokes and Wilson formula [10], as follows:

$$b = b_d + b_e = k\lambda / (d\cos\theta) + 4\varepsilon\tan\theta \quad (3)$$

where, b is the full-width at half-maximum (FWHM) of the diffraction peak after the instrumental correction; b_d and b_e are the FWHM for small grain size and low internal strain, respectively; k is a constant (with a value of 0.9); λ is the wavelength of the X-ray radiation; d and ε are the grain size and the internal strain, respectively; and θ is the Bragg angle. The

parameters b and bs follow Cauchy's form, according to the following relationship: $B_0 = b + b_s$; here, B_0 and b_s are the FWHM of the broadened Bragg peaks and a standard sample's Bragg peaks, respectively. The approximate average grain size of the Cu-coated graphite powder is 3.27 μm.

Fig. 6 shows the TEM imagery of single Cu-coated graphite powder, diffraction pattern, coating thickness and Mapping image. Fig. 6(a) shows the graphite powder and coating layer of copper. The figure shows that the graphite powder, uniform coating layer, and Pt coating layer were gradually stacked uniformly. Fig. 6(b) shows a magnified view of the Cu coating layer to observe the obvious diffraction pattern and Cu coating layer thickness. The diffraction pattern of the Cu coating layer was mixed crystalline and amorphous phase. The thickness of the Cu coating layer formed was almost 316 nm, and oxide film, which is the white area, was formed by the passivation treatment for the prevention of combustion. A result of the mapping image of the Cu coating layer in Fig. 6(c) shows evidence that the layer above the copper layer is oxide film due to oxygen volume. TEM analysis revealed that Cu coatings formed on graphite powder and oxide film were also formed above the copper coatings.

Fig. 7 shows the microstructure of controlled copper-coated graphite powder at different times of 10, 20, and 30 minute by vibrator. Figs. 7(a-c) show the direction controlled Cu-coated graphite powders for 10 min by vibrator were almost irregular direction (Fig. 7(a)), and as the time increased, direction control gradually improved, and the graphite powders showed uniform isotropy. It was revealed that vibration of the Cu coated graphite powder for 30 min had the greatest effect on direction control.

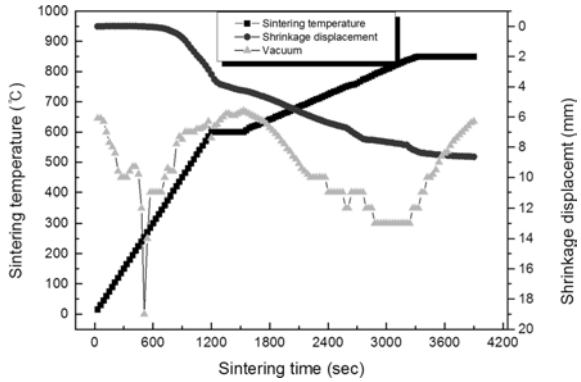

Fig. 8. Variation of shrinkage displacement of Cu-coated graphite compacts with sintering temperature and sintering time during PCAS process under 60 MPa at 850 ºC.

Fig. 8 shows the variations of the shrinkage displacement during the sintering of the Cu-coated graphite powder for which the PCAS process was used. When an electric current was applied, the shrinkage displacement increased by up to 550 ºC, and then abruptly, the shrinkage displacement was nearly constant at above that temperature. When the temperature reached approximately 850 ºC, the densification rate became nearly negligible, and the samples densified to the almost theoretical density at approximately 3,900 sec, as will be further discussed below. The sintered relative densities are 6.128 g/cm^3. These results are attributed to two causes. First, because a high Joule heating

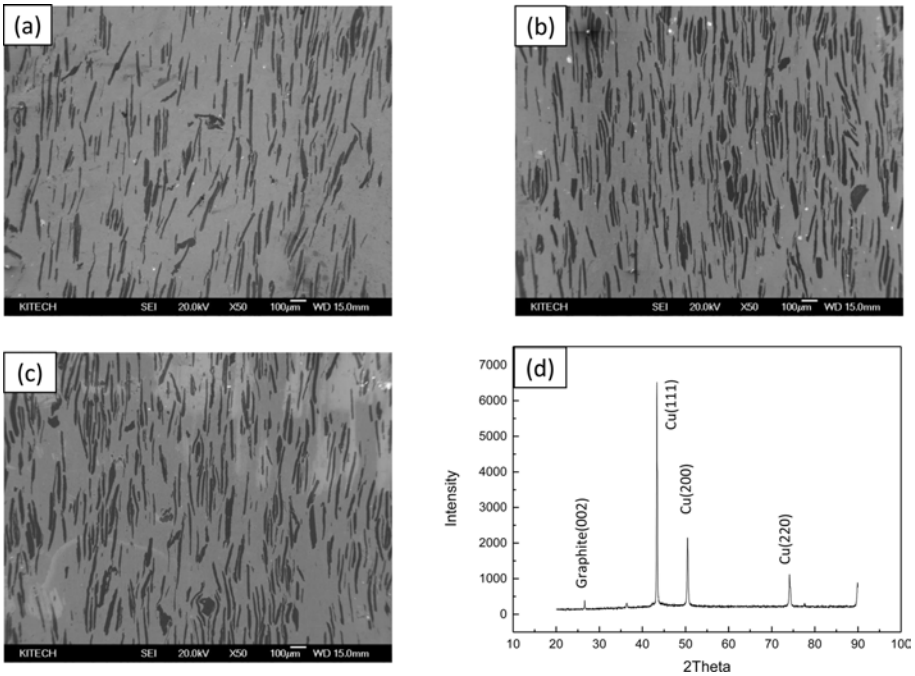

Fig 9. XRD pattern, microstructure of direction controlled copper-coated graphite sintered bodies at different sintering temperature; (a) 250 ºC, (b) 550 ºC, (c) 750 ºC and (d) XRD pattern.

occurs at the point of contact between the particles due to an induced current, the spread of the atoms is accelerated; in addition, the performance of the sintering at low temperature is considered to be easier, because the spread of the atoms is accelerated in an electric field. Second, when pressure is applied during the sintering, the driving force of the sintering is increased; Eq. (2) shows the increased driving force, F, as follows:

$$F_D = \gamma + (P_a r/\pi) \quad (4)$$

where, γ is the interfacial energy, and Pa and r are the applied pressure and the particle radius, respectively. These results suggest that compared with the conventional sintering processes, the most obvious advantages of the PCAS process are faster heating rates, shorter processing times, and relatively lower temperatures during the sintering, all of which allow for the limitation of grain growth and clean grain boundaries [11-12]

Fig. 9 shows the FE-SEM imagery of the polished surfaces for the sample that was heated to 250, 550, and 750 °C at a pressure of 60 MPa. Fig. 9 shows that for each of the sintering temperatures, the microstructure in the FE-SEM imagery consists of the nanophases of the graphite and the copper grain. In Fig. 9(a), the reason for the wide range of graphite particle was that the sintering temperature was not reached, and shrinkage also hardly proceeded.

As the sintering temperature increases (Figs. 9 (b,c)), the distance of the graphite particles reduces. The reason for the abrupt increase of the shrinkage displacement at the ignition temperature is due to the density increase that is the result of the change of molar volume that is associated with the formation of the consolidated Cu-coated graphite sintered bodies.

Fig. 9(d) shows the XRD patterns of the Cu-coated graphite sintered bodies after the PCAS process. All of the peaks are those of Cu and graphite, and impurities are nonexistent.

Fig. 10 shows a magnified view of the content of Fig. 9 by FE-SEM to describe in detail the sinterability according to the temperature. Fig. 10(a) shows that a sintered body at 250 °C was hardly sintered, due to many pores around the graphite particle. Figs. 10(b-c) show almost sufficient sintering. For this reason, it can be seen that as the temperature increases, the sinterability also increases.

The electrical conductivity, thermal conductivity, and thermal coefficients of the Cu-coated graphite sintered bodies along the X-Y axis and X-Z axis directions confirm the direction difference of the graphite material, as shown in Table 1, wherein the electrical conductivity of the X-Y axis, with a minimum of approximately 31.6, increases slightly to a maximum of approximately 38.3; and for the X-Z axis, a minimum of approximately 14.2 increases to a maximum of approximately 15.8. The reason for this behavior was that the X-Y axis shows low electrical conductivity, because the former is equipped with electrically charged electrons to move electrons through the Van der Waals force, whereas the X-Z axis has a share of its own, preventing the electron from moving

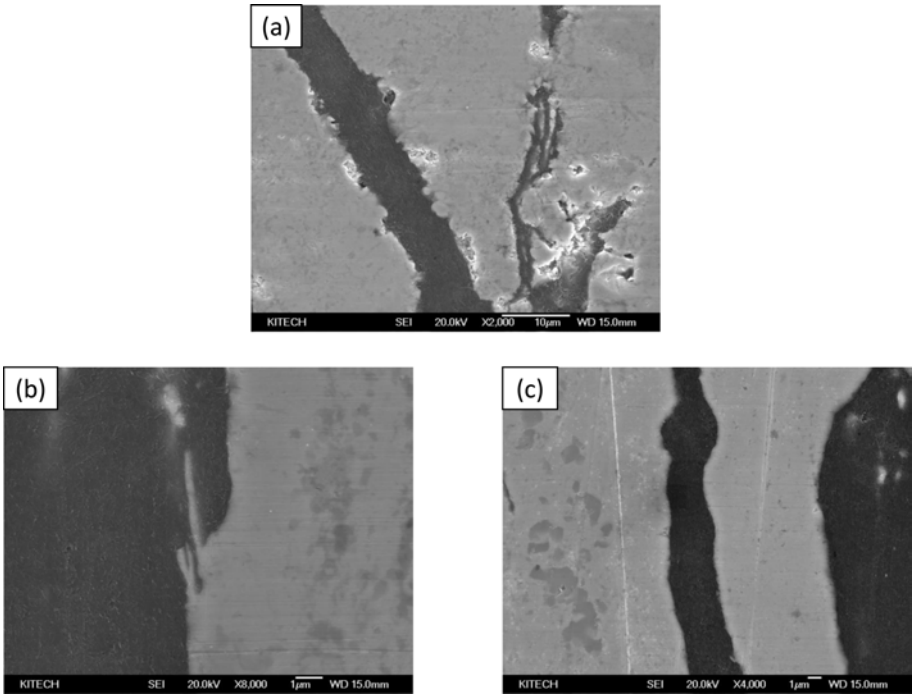

Fig. 10. High magnification microstructure of direction controlled copper-coated graphite sintered bodies at different sintering temperature; (a) 250 °C, (b) 550 °C and (c) 750 °C.

Table 1. Result of thermal properties and electrical conductivity cu-coated compacts for different measuring temperature; (a) Electrical conductivity, thermal coefficient and thermal conductivity according to difference of temperature and (b) thermal diffusivity according to difference of temperature.

(a)

Direction control	Room temperature T. C. (W/mK)	50 °C T. C. (W/mK)	100 °C T. C. (W/mK)	Electrical conductivity (100% IACS)	Therma coefficien (E^{-6})
X-Y axis	104.0	102.6	101.5	31.6 ~ 38.3	11.73
X-Z axis	496.4	461.2	408.3	14.2 ~ 15.8	11.73

(b)

Direction control	Room temperature T. C. (W/mK)	50 °C T. C. (W/mK)	100 °C T. C. (W/mK)
X-Y axis Thermal diffusivity	37.7	36.4	34.5
X-Z axis Thermal diffusivity	180.0	163.6	138.8

independently.

Table 1 shows the thermal conductivity of the Cu-coated graphite sintered bodies along the X-Y and X-Z axis directions for different measuring temperatures. The thermal conductivity equation is as follows:

$$K = a*C_p*\rho \quad (5)$$

where, a is the diffusivity (mm^2/s), C_p is the specific heat, and ρ is the density[13]. The thermal conductivity value was thrice higher than that in the case of being oriented to the X-Z axis when oriented to the X-Y axis. In the case of graphite oriented to the X-Z axis, which is the covalent bond, the thermal diffusivity is higher than for the X-Y axis, which is the Van der Waals force due to the interstitial spacing being too narrow. Table 1 (b) shows the difference of thermal diffusivity along the X-Z and X-Y axes. The density of sample of the X-Z axis and X-Y axis is 6.128 g/cm^3, and the specific heat of the sample of the X-Z axis and X-Y axis is 0.45, 0.46, and 0.48 at room temperature, 50 °C, and 100 °C, respectively. While the highest thermal conductivity was achieved at room temperature, the thermal conductivity of the sintered bodies was almost the same; however, for the Cu-coated graphite sintered bodies, the direction controlled Cu-coated graphite powder can achieve the highest and most reasonable material.

Conclusions

The results of the particle size analysis show that the particle size of the Cu-coated graphite powder decreased from the initial graphite powder due to the mixture of transposed Cu ion. The XRD patterns show that only the graphite (006) and Cu (111), (200), and (220) peaks were observed, and no impurity was detected. The results of TEM analysis confirmed that graphite powder, Cu coating layer, and oxide film were stacked gradually. For direction control, the vibration time of Cu coated graphite powder of 30 min produced the greatest effect. The density of the compact sintered body was 6.128 g/cm^3 at 850 °C. The electronic conductivity results, for which the sintered samples were used, show that the Van der Waals force on the X-Y axis resulted in higher directionality than the covalent bond of the X-Z axis, due to the existent electrons. However, the thermal conductivity results of the Van der Waals force of the X-Y axis (101.5 ~ 104.0) resulted in a lower directionality than the covalent bond of the X-Z axis (408.3 ~ 496.4), due to the reduced lattice spacing.

Acknowledgments

This study has been conducted with the support of the Korea Institute of Industrial Technology as “Source technology development project (KITECH EO-18-0002)”.

Reference

1. H. Wang, F. Wang, Z. Li, Y. Tang, B. Yu and W. Yuan, Applied Energy 176 (2016) 221-232.
2. R. Mahajan, R. Nair, V. Walkharkar, Intel. Technol. J. 6 (2002) 55-61.
3. M. Hodes, R.D. Weinstein, S.J. Pence, J. Electron Package 124 (2002) 419-426.
4. T.J. Lu, Int. J. Heat Mass Transf. 43 (2000) 2245-2256.
5. D. Yoo, Y.K. Joshi, IEEE Trans. Dev. Mater. Reliab. 4 (2004) 641-649.
6. R. Kandasamy, X.Q. Wang, A.S. Mujumdar, Appl. Therm. Eng. 27 (2007) 2822-2832.
7. J.H. You, Nuclear Materials and Energy 5 (2015) 7-18.
8. A. Ebrahimi, A. Dadvand, Alexandria Engineering Journal

54 (2015) 1003-1017.
9. S.B. Yang, B.K. Min, D.H. Jung, S.D. Choi, Journal of the Institute of Industrial Technology 28 (2000) 95.
10. F.L. Zhang, C. Wang, M. Zhu, Scripta Mater. 49 (2003) 1123-1128.
11. A. Morell, A. Mermosin, Bull. Am. Ceram. Soc. 59 (1980) 626-629.
12. K. Jia, T.E. Fischer, G. Gallois. Nanostruct. Mater. 10 (1998) 875-891.
13. ISO22007-4:2008 Plastics-Determination of thermal conductivity and thermal diffusivity-Part 4: Laser flash method.